The Journal of Experimental Biology 205, 1709–1724 (2002)
Printed in Great Britain © The Company of Biologists Limited
JEB4064

Hydrodynamics of caudal fin locomotion by chub mackerel, *Scomber japonicus* (Scombridae)

Jennifer C. Nauen* and George V. Lauder

Department of Organismic and Evolutionary Biology, Harvard University, 26 Oxford Street, Cambridge, MA 02138, USA

*e-mail: jnauen@oeb.harvard.edu

Accepted 13 March 2002

Summary

As members of the derived teleost fish clade Scombridae, mackerel exhibit high-performance aquatic locomotion *via* oscillation of the homocercal forked caudal fin. We present the first quantitative flow visualization of the wake of a scombrid fish, chub mackerel *Scomber japonicus* (20–26 cm fork length, *FL*), swimming steadily in a recirculating flow tank at cruising speeds of 1.2 and 2.2 *FL* s^{-1}. Thrust was calculated from wake measurements made separately in the horizontal (frontal) plane and vertical (parasagittal) planes using digital particle image velocimetry (DPIV) and compared with drag measurements obtained by towing the same specimens of *S. japonicus post mortem*.

Patterns of flow indicated that the wake consisted of a series of linked elliptical vortex rings, each with central jet flow. The length of the minor axis (height) of the vortex rings was approximately equal to caudal fin span; the length of the major ring axis was dependent on swimming speed and was up to twice the magnitude of ring height. Profiles of wake velocity components were similar to theoretical profiles of vortex rings.

Lift, thrust and lateral forces were calculated from DPIV measurements. At 1.2 *FL* s^{-1}, lift forces measured relative to the *X* axis were low in magnitude (–1±1 mN, mean ± S.D., *N*=20) but oriented at a mean angle of 6° to the body axis. Reaction forces tend to rotate the fish about its center of mass, tipping the head down. Thus, the homocercal caudal fin of *S. japonicus* functions asymmetrically in the vertical plane. Pitching moments may be balanced anteriorly *via* lift generation by the pectoral fins. Thrust estimates for the two smallest fish based on DPIV analysis were not significantly different from drag measurements made by towing those same animals. At a speed of 1.2 *FL* s^{-1}, thrust magnitude was 11±6 mN (mean ± S.D., *N*=40). Lateral force magnitudes were approximately double thrust magnitudes (22±6 mN, mean ± S.D., *N*=20), resulting in a mean mechanical performance ratio (thrust/total force) of 0.32 at 1.2 *FL* s^{-1}. An increase in speed by a factor of 1.8 resulted in a mean increase in thrust by a factor of 4.4, a mean increase in lateral forces by a factor of 3, no change in the magnitude of lift produced and an increase in mean mechanical performance to 0.42. The relatively high lateral forces generated during swimming may be a necessary consequence of force production *via* propagated waves of bending.

Movies available on-line.

Key words: hydrodynamics, locomotion, swimming, scombrid, fish, force balance, mackerel, *Scomber japonicus*.

Introduction

Fish move by transferring momentum to the surrounding fluid; thus, patterns of flow in the vicinity of freely swimming fish, including the boundary layer and wake, are of interest to those studying aquatic locomotory mechanisms. Technological advances over the last decade now allow investigators to quantify flow characteristics in the vicinity of freely swimming fish using digital particle image velocimetry (DPIV). Flow is visualized by the addition of reflective, inert, near-neutrally buoyant particle markers to the fluid, and flow-field characteristics including velocity and vorticity are calculated from successive images of flow captured at high frequency (Raffel et al., 1998). DPIV has become the method of choice to analyze complex flow fields generated by aquatic animals. Wakes of larval (Müller et al., 2000) and adult (Stamhuis and Videler, 1995; Müller et al., 1997, 2000; Drucker and Lauder, 1999, 2000, 2001a; Wilga and Lauder, 1999, 2000; Hanke et al., 2000; Lauder, 2000) fishes, flow fields along the body of swimming fish (Anderson et al., 2000; Nauen and Lauder, 2001a) and feeding and ventilatory currents of copepods and shrimp (Stamhuis and Videler, 1995) have been quantified using DPIV.

In the present study, we use DPIV to describe the wake morphology and force balance for chub mackerel *Scomber japonicus* (Teleostei: Scombridae). *S. japonicus* is a basal

member of the family Scombridae, a group that includes the high-performance bonitos and tunas and is characterized by a streamlined body and an externally symmetrical or homocercal caudal fin. Steady swimming kinematic patterns of mackerel are typically classified as characteristic of the carangiform swimming mode (Lindsey, 1978), in which lateral body oscillations are largely restricted to the posterior third of the body, with large lateral oscillation amplitudes by the caudal peduncle and fin (see, for example, Gibb et al., 1999; Donley and Dickson, 2000; Nauen and Lauder, 2001a). The anterior body segments of *S. japonicus* undergo small lateral oscillations (amplitudes <2.5 % of total body length) during steady swimming, and oscillation amplitude increases approximately exponentially over the posterior third of the body (see Fig. 6A in Donley and Dickson, 2000). Thus, in contrast with anguilliform locomotion, where much of the body undergoes large lateral oscillations (Lindsey, 1978; Gillis, 1998) and produces hydrodynamic force during steady swimming, (Müller et al., 2001), the primary site of hydrodynamic force production for *S. japonicus* is the posterior third of the body, including the caudal peduncle and particularly the caudal fin.

As scombrid fishes are noted for their high-performance steady locomotion (see, for example, Fierstine and Walters, 1968; Magnuson, 1978; Wardle and He, 1988), one goal of this project was to describe the wake produced by a scombrid fish during steady swimming. These data can be compared with previous data on wakes produced during caudal fin locomotion by mullet (Müller et al., 1997), eel (Müller et al., 2001), giant danio (Anderson, 1996; Wolfgang et al., 1999), sturgeon (Liao and Lauder, 2000) and bluegill sunfish (Drucker and Lauder, 2001b). Since all previous quantitative data on caudal fin wake structure have been obtained from an analysis of either the horizontal (frontal, *XZ*) or vertical (parasagittal, *XY*; Fig. 1) plane at a single swimming speed, a second goal of the project was to determine the effect of speed on wake characteristics. We collected data at both relatively slow and fast steady cruising speeds (1.2 and 2.2 fork lengths s^{-1}, respectively, where *FL* is fork length).

Wake morphology measurements were made in both the horizontal (*XZ*) and vertical (*XY*) planes (Fig. 1) to provide two separate measurements of wake morphology (and thus thrust production) from orthogonal light-sheet orientations. By inducing fish to swim steadily at different heights in the water, we altered the position of the caudal fin relative to the horizontal light sheet and were thus able to characterize the wake shed by different areas of the caudal fin. DPIV thrust measurements at a steady swimming speed of 1.2 *FL* s^{-1} were compared with drag measurements made by towing the same individuals (*post mortem*) at that speed. To establish the mechanical performance of the homocercal mackerel tail in the horizontal plane, we determined the ratio of thrust to total force produced during steady swimming.

Characterizing the wake of *Scomber japonicus* also allowed us to address questions concerning the magnitude and orientation of hydrodynamic forces produced by a homocercal caudal fin of a teleost fish. The symmetrical morphology of the homocercal tail has led to the assumption that, during steady swimming, forces are generated only in the horizontal plane and that no is lift produced (for a review, see Lauder, 2000). Mackerel have negatively buoyant bodies (Magnuson, 1973) that require lift production for steady horizontal swimming. Three sources of lift traditionally identified for scombrids are the pectoral fins, body and caudal keels (summarized by Magnuson, 1978). However, a recent kinematic study of steady swimming by *S. japonicus* showed that the caudal fin is tilted at an angle of up to 10 ° relative to the vertical and its movement is thus asymmetrical (Gibb et al., 1999), suggesting that the caudal fin of *S. japonicus* may produce lift during steady swimming. To address this question, we used DPIV data from the vertical plane to measure the angle of the reaction force on the body relative to the center of mass.

Materials and methods

Animals

Chub mackerel, *Scomber japonicus* (Houttuyn), were collected by hook and line at several locations in coastal southern California (USA). The fish were fed chopped fish and housed in 1200 l tanks at a water temperature of 18±2 °C in a 12 h:12 h light:dark photoperiod.

Flow visualization

Experiments were conducted using a 600 l recirculating salt-water flow tank at 19±1 °C. The flow tank has a working area 82 cm long by 28 cm wide by 28 cm high; flow speed in the tank was controlled using a variable-speed motor. Details of the flow tank and flow speed calibration have been presented previously (Jayne et al., 1996; Gibb et al., 1999). We used a flow tank, rather than have mackerel swim across the field of view of the cameras in still water conditions, to control the speed of the fish and use a relatively small field of view (approximately 10 cm×12 cm) to provide a high-resolution view of the wake.

As in previous studies of flow visualization from our laboratory (Drucker and Lauder, 1999, 2000; Wilga and Lauder, 1999, 2000; Lauder, 2000; Nauen and Lauder, 2001a), flow was visualized by seeding the water with near-neutrally buoyant silver-coated glass beads 12 µm in diameter (density 1.3 g cm^{-3}; Potters Industries, USA) that reflected light from a 5 W argon-ion laser (Fig. 1). Examples of particle density are shown in Fig. 1A,B. The laser light sheet was approximately 2 mm thick and 10 cm wide. It was positioned in the center of the working section of the flow tank and oriented in either the vertical (parasagittal, *XY*, Fig. 1) or horizontal (frontal, *XZ*) plane. The vertical light sheet was projected from below the tank (Fig. 1). The horizontal sheet was projected from the left side of the tank; a ventral view of the horizontal light sheet (Fig. 1B) was recorded with a camera that viewed a front-surface mirror set at 45 ° beneath the tank.

Images of the fish were recorded at 250 Hz using one camera of a two-camera synchronized NAC high-speed video system;

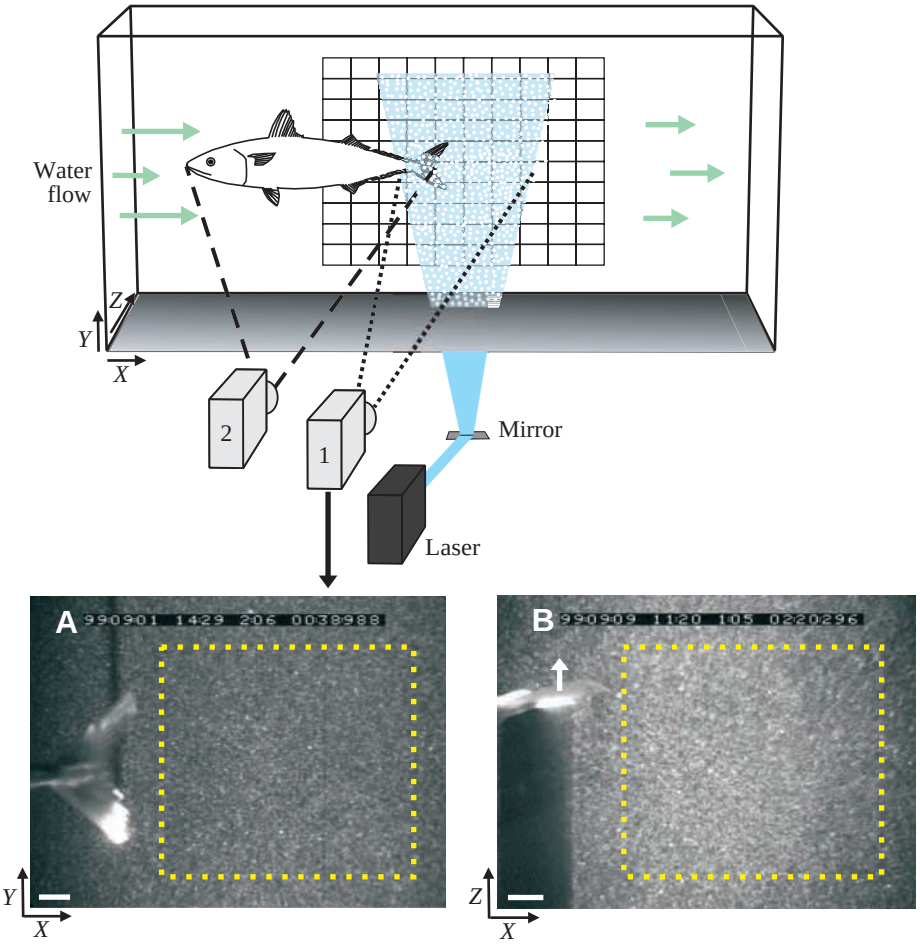

Fig. 1. Mackerel swam at a constant speed of 1.2 or 2.2 *FL* s^{-1}, where *FL* is fork length, in a flow tank, and a laser light sheet oriented in the vertical (parasagittal, *XY*) (shown) or horizontal (frontal, *XZ*) plane illuminated small particles in the flow. Camera 1 recorded images of the caudal fin and the area of the light sheet posterior to it; in the example shown in A, the tail is beating out of the plane of the light sheet towards the reader with the caudal fin tilted at an acute angle to the *Y* axis (as also shown by Gibb et al., 1999). The ventral lobe of the caudal fin, illuminated by the light sheet, is trailing the dorsal lobe, which has previously passed through the sheet. Camera 2 recorded synchronous images of the body of the mackerel that were used to determine the orientation of the body to the *X* axis. Images of the light sheet oriented in the *XZ* plane (B) were recorded from below the tank using a front-surface mirror. Note that the caudal peduncle and fin blocked the light sheet as they moved through it (the arrow in B indicates the direction of fin movement), creating a shadow (seen, for example, in B). Yellow dotted lines in A and B outline the approximate image area analyzed using digital particle image velocimetry. The white scale bars in the lower left of A and B represent 1 cm.

these images were used to determine the fish's position relative to the light sheet and the angle of the body to the *X* axis (defined in Fig. 1). A second camera viewed the movement of particles illuminated by the light sheet. The cameras' fields of view were calibrated by recording images of a ruler at the beginning of each experiment. Note that as the caudal fin moved across the field of view it blocked portions of the light sheet (which resulted in dark areas in the images; e.g. Fig. 1A,B).

Three *Scomber japonicus* (fork length 22 cm, 24 cm and 26 cm) were used for both horizontal and vertical light-sheet experiments. One other individual (23 cm fork length) was used for horizontal light-sheet experiments only. A final individual (20 cm fork length) was used for vertical light-sheet experiments only. Fish swam at speeds of 1.2 *FL* s^{-1} (the lowest speed at which steady swimming was observed) and 2.2 *FL* s^{-1}. These speeds are within the range of swimming speeds Atlantic mackerel can sustain for longer than 200 min (0.4–3.5 total lengths s^{-1}, where *TL* is total length; Wardle and He, 1988), are well below the maximum sustainable swimming speeds of 4–5 *FL* s^{-1} for *S. japonicus* of this size (Sepulveda and Dickson, 2000) and match speeds used in a previous study of *S. japonicus* caudal fin kinematics (Gibb et al., 1999).

To obtain accurate force measurements for steady swimming from the DPIV data (see below), video sequences were analyzed only when mackerel were holding position for several strokes and not drifting either vertically or laterally because even small deviations from steady swimming produced markedly different flow patterns in the wake. Measurements of body angle to the *X* axis were obtained at the time the vortex of interest was shed from the caudal fin by analyzing video images of mackerel body position obtained by the second video camera synchronized with the DPIV recordings (Fig. 1). Stroke duration was determined as the time between maximum excursions of the caudal fin in the *XZ* plane.

Digital particle image velocimetry (DPIV)

DPIV methods have been described in detail previously (Willert and Gharib, 1991; Anderson, 1996; Raffel et al., 1998); the specific methods used in the present study are based on previous studies on the wakes of fish conducted in our laboratory (e.g. Drucker and Lauder, 1999; Lauder, 2000; Liao and Lauder, 2000; Wilga and Lauder, 2000). Video images were imported into a PC computer using DT-Acquire software with a Data Translation video card (Data Translation, Inc., USA). Using Insight software (v. 3; TSI, Inc., USA), selected areas (e.g. Fig. 1A,B) of sequential pairs of video images (4 ms apart in time) were analyzed by subdividing the analysis area of interest into a series of interrogation windows and comparing these data subsets using two-frame cross-

correlation analysis. The areas of flow analyzed here were typically rectangular in shape and were thus analyzed with a grid of 40×30 vectors. The cross-correlation analysis used a fast-Fourier transform correlation process with a Gaussian peak search algorithm, a spot size of 64 pixels and a peak signal-to-noise ratio of 1.5.

Vector trajectories and mean velocities were calculated trigonometrically from orthogonal velocity components using Transform (v. 3.3; Fortner Research LLC, USA). To determine vortex geometry, average free-stream velocity was subtracted from each vector to reveal vortical structures (e.g. Fig. 2). Velocity gradients across the wake were examined to compare vortex morphology with theoretical patterns.

More than 200 pairs of images were analyzed using DPIV (at least 12 pairs for each fish at each speed for each of the *XY* and *XZ* views of the wake). At the relatively slow speed of 1.2 $FL\,s^{-1}$ (absolute speeds of 26.4–31.2 $cm\,s^{-1}$), background turbulence was low and flow data were of high quality, resulting in 10 (five for each light sheet) very good DPIV analyses for each fish (see Table 1). This sample size was sufficient for statistical analysis. At the speed of 2.2 $FL\,s^{-1}$ (48.4–57.2 $cm\,s^{-1}$), high background turbulence obscured many images of the wake. Thus, only 12 horizontal light-sheet and seven vertical light-sheet images of good quality were obtained from the more than 100 pairs of images analyzed. The 2.2 $FL\,s^{-1}$ data set is presented in Table 1 and Figs 4, 6 and 7, but the data set was not large enough for statistical comparison with 1.2 $FL\,s^{-1}$ data.

DPIV measurements and force calculations

Circulation of vortices in the wake was used to infer propulsive forces on the caudal fin that arise from circulation about the fin. This inference is justified by equivalence in the absolute magnitude of bound and shed circulation during the impulsive start of a hydrofoil (according to Kelvin's theorem; Milne-Thompson, 1966; Dickinson, 1996), such as that observed during caudal fin acceleration, which occurs during the first half of each stroke by *Scomber japonicus* (Nauen and Lauder, 2000). The methodology applied here was used successfully to estimate the force produced during pectoral fin locomotion by the bluegill sunfish *Lepomis macrochirus* (Drucker and Lauder, 1999).

Assuming that all the momentum added to the fluid by the fish is contained in vortices in the wake, the time-averaged locomotor force F can be calculated as:

$$F = \rho\Gamma A/T, \quad (1)$$

where ρ is the density of salt water (1024 $kg\,m^{-3}$ at 20 °C), Γ is the circulation (the line integral of the tangential velocity component V about a curve C enclosing the vortex; Batchelor, 1967), A is the projected area of a vortex ring in the laser plane and T is the time over which force is generated. Γ was determined using a custom-designed computer program in which the user defined a circular integration path C around each vortex center on the 40×30 vector matrix. Γ was calculated at increasing integration path radii (0.2 cm increments) across the vortex until asymptotic values of circulation were reached. At that point, the path radius equaled the vortex core radius (for more details, see Drucker and Lauder, 1999).

The distance between the centers of the vortices (representing ring width in the horizontal plane and ring height in the vertical plane), and the angle φ between the X axis of the vector map (defined in Fig. 1) and the ring axis or the jet, were measured from the vector plots using Scion Image (Scion Corp, USA). A mean value of ring area (calculated as the area of an ellipse) was calculated for each swimming speed and used in the force calculation described above because ring height and ring width could only be measured from either the vertical and horizontal light sheets, respectively, and the distance between vortex centers was independent of individual (see Table 2). Stroke duration was defined as the time between points of maximum stroke amplitude and was determined from video images of the ventral aspect of the mackerel (horizontal light-sheet data only). A mean value of stroke duration was calculated for each speed and used in the force calculation described above because stroke duration was independent of individual (analysis of variance, F=2.0, P=0.15).

Drag measurements

The total drag of *post-mortem Scomber japonicus* was measured using a force transducer to compare with estimates of thrust calculated from the DPIV measurements. The technique used was similar to that of Drucker and Lauder (1999). A flexible vertical rod secured from above was placed so that the fish was suspended in the center of the tank. Individuals were attached to the rod *via* suture line threaded through the jaws and skull; the mouth was fixed in place slightly open to ensure a flow of water through the branchial cavity. All the fish used in the study were tested at flow speeds equal to swimming speeds of 1.2 and 2.2 $FL\,s^{-1}$; however, the fish were only stable at relatively low flow speeds. At higher flow speeds, excessive flutter of the fish body on the line precluded accurate drag estimates, and the data were discarded. Thus, the drag measurements presented here are for the two smallest fish (fork length 20 and 22 cm) at the speed of 1.2 $FL\,s^{-1}$.

Rod bending (measured as displacement at the rod tip) due to the drag of the fish was recorded using high-speed digital video (Redlake Corp.) and measured using the Scion Image digitizing program. Bending of the unloaded rod in flow was also recorded, measured and subtracted from that of the loaded rod to account for the small amount of drag due to the transducer in the flow. Three independent tests were conducted for all the measurements. Rod displacement was recorded for 10 s at 60 Hz. More than 40 images from that series were randomly selected, rod displacement was measured from those images and a mean displacement value was calculated.

The transducer was calibrated before and after the experiment by clamping the rod horizontally and hanging a range of masses (0.4–10 g, corresponding to 3.9–98 mN) from it so that the masses pulled on the bar in the same manner as

Table 1. *Kinematic and wake parameters during locomotion by* Scomber japonicus *at speeds of 1.2 and 2.2* FL *s*$^{-1}$

	1.2 *FL* s^{-1}		2.2 *FL* s^{-1}	
Parameter	Horizontal[a]	Vertical[a]	Horizontal[b]	Vertical[c]
Stroke duration (ms)	200±24	–	119±8	–
Body angle to horizontal (degrees)	–	–3±4	–	–4±4
Vortex radius (cm)	0.82±0.26	0.78±0.23	0.93±0.08	0.83±0.26
Distance between vortex centers (cm)	5.49±0.71	3.25±0.66	6.79±1.05	3.54±0.49
Ring axis angle (degrees)	34±10	86±13	27±5	91±7
Jet angle (degrees)	67±9	–3±5	53±12	–2±4
Circulation (cm^2 s^{-1})	31±9	15±8	52±8	27±11
Momentum (g cm^2 s^{-1})	437±123	210±110	1001±157	529±208
Lateral force (mN)	22±6	–	65±14	–
Vertical force (mN)	–	–1±1	–	–1±2
Downstream force (mN)	10±5	11±6	50±16	44±17
Mean downstream force/mean lateral force	0.5	NA	0.77	NA
Total force (mN)	24±7	11±6	84±13	44±17

Values are presented as means ± S.D.

[a]*N*=20 (five strokes from each of four fish); [b]*N*=12 (at least one stroke from each of four fish); [c]*N*=7 (at least one stroke from each of four fish).

FL, fork length.

NA, not applicable.

the drag from the fish. The transducer showed a linear response in the range of loads measured and no change in response due to the load of the fish. Because of the averaged nature of the rod displacement measurements, all force measurements were rounded to the nearest mN.

Statistical analyses

Statistical analyses were performed using SuperANOVA (v. 1.11) on kinematic and flow data for five strokes from each of four fish (*N*=20) swimming at 1.2 *FL* s^{-1}. As stroke duration and lateral forces were determined from the horizontal light-sheet data only, and the angle of the body to the *X* axis and vertical forces were determined from the vertical light-sheet data only, single-factor analysis-of-variance (ANOVA) tests were performed to determine the effect of individual on these variables. All other wake variables (see Table 1) were determined from data collected with both light sheets, so two-factor ANOVAs were performed in which light-sheet orientation was a fixed factor and individual was a random factor (see Table 2). All *F* values were calculated as described by Zar (1984). To correct for performing multiple tests on the data set, the Bonferroni correction of $P=0.05/k$, where *k* is the number of variables analyzed (Rice, 1989), was applied (as previously; see Nauen and Lauder, 2001b). Regression relationships were calculated using Statgraphics (v. 3; Manguistics Corp.). Force values calculated from DPIV data showed significant differences in variance from force data measured with the transducer (Bartlett's test; *P*=0.003 for the 20 cm fish and *P*=0.007 for the 22 cm fish). Therefore, median values of force were compared using the Kruskal–Wallis comparison of median values test (Zar, 1984).

Results

Swimming kinematics

Kinematic data are summarized in Table 1. At a speed of 1.2 *FL* s^{-1}, mean values of stroke duration were 200±24 ms (mean ± S.D., *N*=20, Table 1) and were independent of individual (ANOVA, *F*=2.0, *P*=0.15). Stroke duration decreased at the higher swimming speed of 2.2 *FL* s^{-1} (119±8 ms, mean ± S.D., *N*=12, Table 1). Thus, mean tailbeat frequencies were 2.5 Hz and 4.2 Hz at swimming speeds of 1.2 and 2.2 *FL* s^{-1}, respectively. Mackerel tended to swim with their bodies tilted slightly head-down [the angle of the body to the horizontal was –3±4 ° (mean ± S.D., *N*=20) at 1.2 *FL* s^{-1} and –4±4 ° (mean ± S.D., *N*=7) at 2.2 *FL* s^{-1}]. The magnitude of tilting varied among individuals (ANOVA, *F*=120.0, *P*=0.0001).

General wake structure

Viewed in either the horizontal or vertical plane, the wake consisted of a series of strong counter-rotating vortices (Fig. 2) typical of the structure of a series of linked vortex rings. Between each pair of counter-rotating vortices, a jet of high-velocity flow was formed. Correlating movement of the caudal fin along the *Z* axis with patterns of flow in the wake (the time series in Fig. 2) indicates that a vortex was shed from the caudal fin during the first quarter of each stroke.

As a test of vortex ring height, horizontal (*XZ*) light-sheet data were collected at the dorsal tip of the caudal fin, at the middle of the dorsal lobe of the fin and at the midpoint or 'V' of the fin (Fig. 3). At the dorsal tip of the fin (Fig. 3A), essentially no vorticity was seen. When the middle of the caudal fin's upper lobe (Fig. 3B) and the midpoint of the caudal fin (Fig. 3C) beat through the light sheet, a series of vortices was

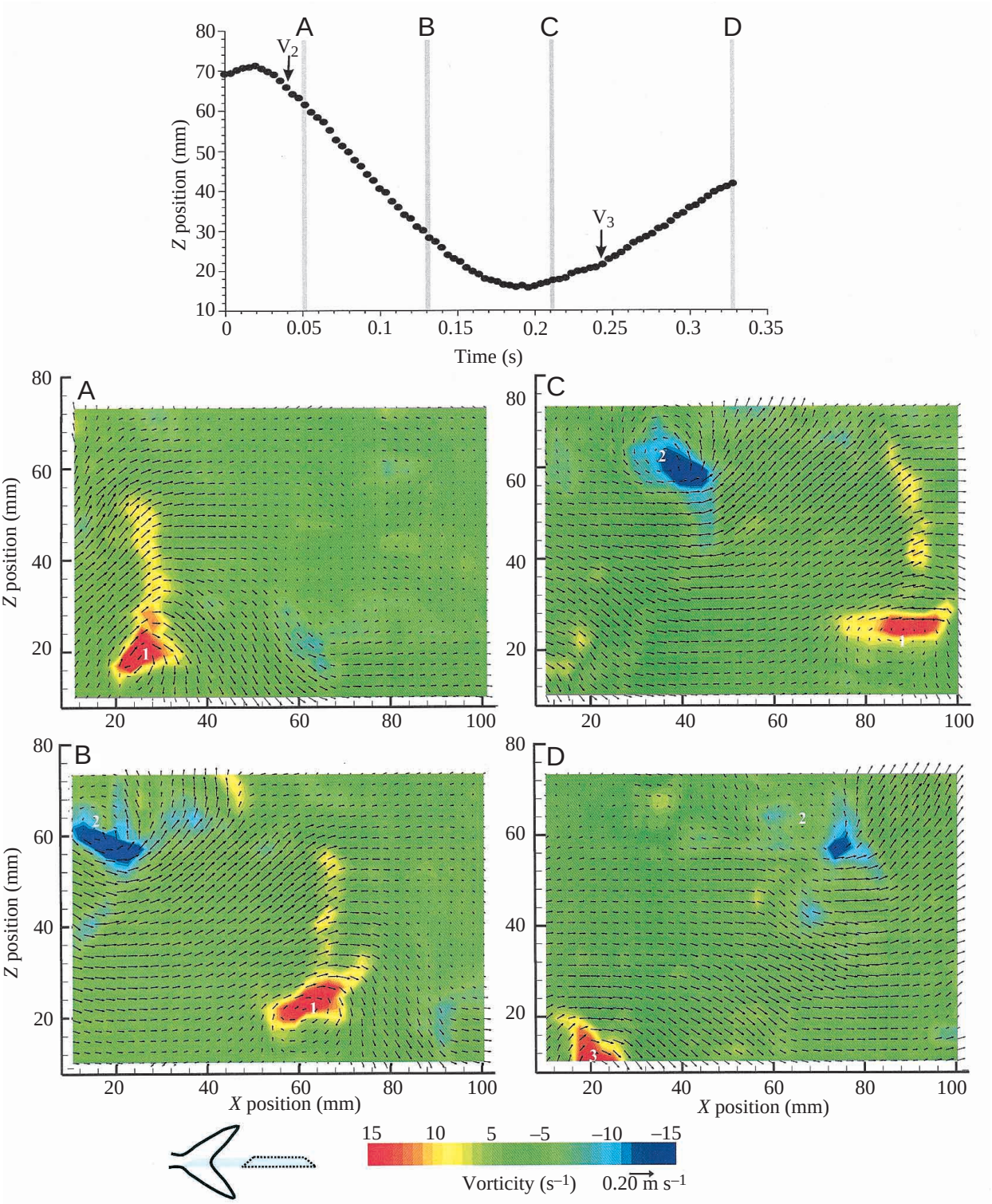

Fig. 2. The time course of vortex production over approximately one tail beat of a *Scomber japonicus* 24 cm in fork length (*FL*) swimming at 1.2 *FL* s^{-1}. The distal tips of the caudal fin were positioned approximately 1 cm to the left of the flow fields shown (see Fig. 1B for an example of caudal fin position and image region analyzed). The caudal fin was moving through the horizontal (*XZ*) light sheet at the position of the fin's lateral midline (as confirmed by camera 2, see Fig. 1, and shown in the diagram of the caudal fin and light sheet). Fin position relative to the *Z* axis was determined at 4 ms time intervals. Arrows in the time series indicate times at which a vortex could first be seen distinct from the caudal fin; gray columns indicate the time of the wake images presented below. Flow velocity is represented by the black vectors plotted over a color background indicating flow vorticity. Vortices in the wake are numbered consecutively in the order in which they are shed from the caudal fin. V_2, V_3, vortices 2 and 3. Note that the vortex number is placed approximately in the center of the vortex (as defined by vector orientation), which does not necessarily correspond with the area of highest vorticity (i.e. the region of most intense red or blue color).

seen (Fig. 2). Thus, vortex ring height was approximately equal to caudal fin span. The jet formed between the pairs of counter-rotating vortices showed some continuity between vortex pairs (see Fig. 3C) but had a strong lateral component (e.g. Fig. 2C).

Analysis of flow in the vertical (*XY*) plane showed a series of counter-rotating vortex pairs (Fig. 4), each with a central jet of flow in the wake. At both slow ($1.2\,FL\,s^{-1}$, Fig. 4A) and relatively fast ($2.2\,FL\,s^{-1}$, Fig. 4B) cruising speeds, the main axis connecting the centers of the counter-rotating vortices (see Fig. 4B) was approximately perpendicular to the *X* axis, and jet trajectory was approximately horizontal. Note that the relatively strong lateral component of the jet seen in the *XZ* plane images of Figs 2 and 3 is not present in the vertical light-sheet images because that flow is out of the plane of the vertical light sheet.

Profiles of wake velocity components were very similar to theoretical profiles for isolated vortex rings (Fig. 5). The left panels of Fig. 5 show three theoretical velocity profiles across *XY* planar sections of the wake. The right panels contain raw empirical data from this study calculated from a high-resolution 50×50 vector field. *X*′ is the longitudinal axis of the ring; *Y*′ is perpendicular to *X*′ (see Fig. 4B for an illustration of the axes described here). The components of velocity parallel to *X*′ and *Y*′ are *u*′ and *v*′, respectively. Fig. 5A is a longitudinal velocity profile of the wake at the midpoint of the vortex cores. Fig. 5B is a velocity profile across the ring's central axis or jet; Fig. 5C is a velocity profile across a single vortex core. In all the profiles, velocity is high at the edges of a vortex core or at the midpoint between the two vortices. The peak in velocity at the midpoint between two vortices reflects the strength of the central jet. In general, the empirical data and theoretical profiles agree, indicating that the vortices viewed are part of vortex rings. The fact that velocity is greater than zero at the jet margins (rather than decreasing to zero as in the theoretical profile in Fig. 5B) indicates that these rings are part of a vortex chain (depicted in Fig. 8) rather than single, isolated rings. Similarly, the experimental data in Fig. 5C do not reach the zero point at the vortex margins because of the velocity imparted by upstream and downstream linked rings.

Vortex orientation and geometry

On average, vortex core radii were slightly less than 1 cm (Table 1) at both the slow and fast speeds. As vortex radius was independent of light-sheet orientation (P=0.381, Table 2), as well as individual (P=0.519, Table 2) and interaction (P=0.499, Table 2) effects, the

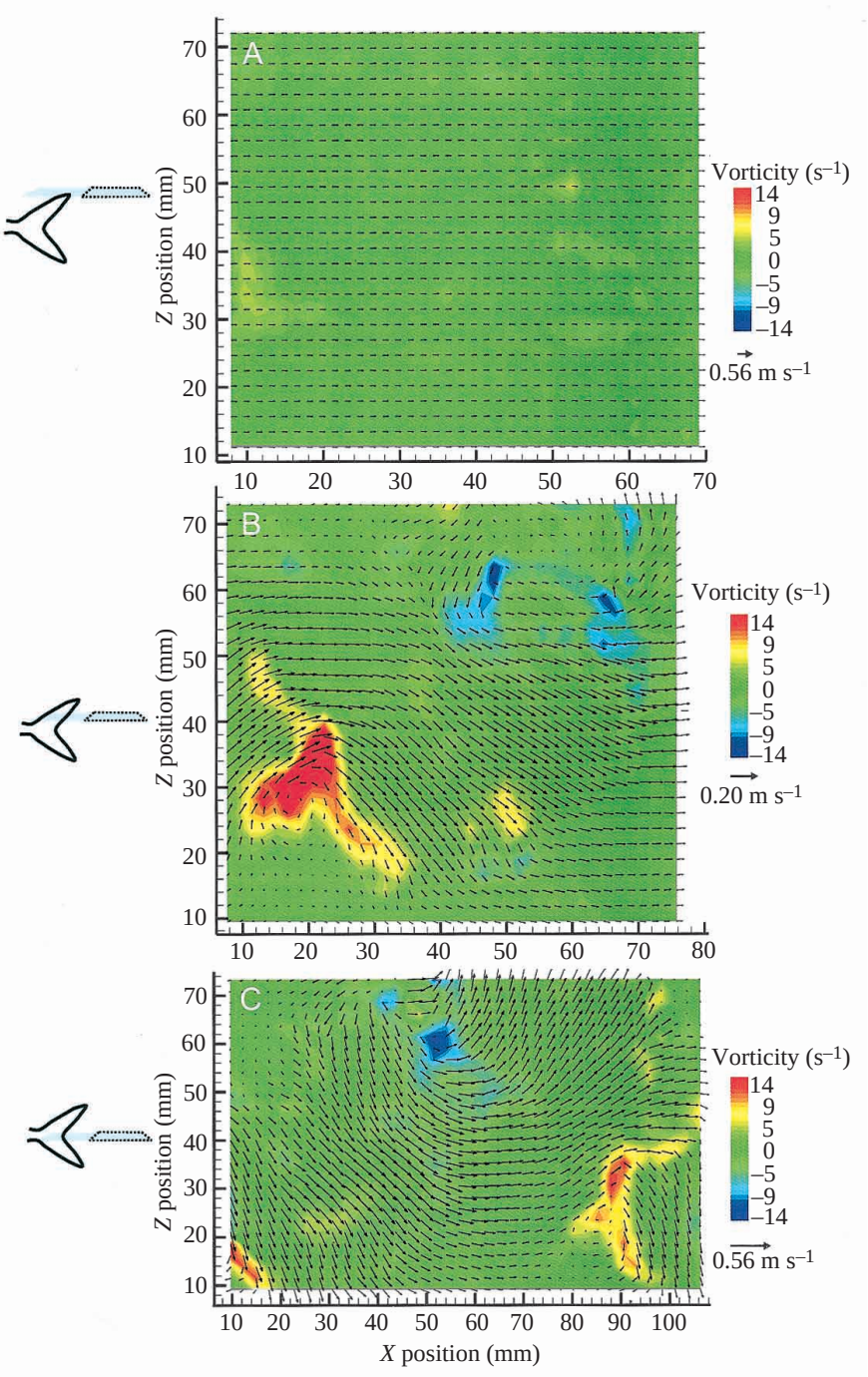

Fig. 3. Views in the horizontal (*XZ*) plane of the wake of a *Scomber japonicus*, 24 cm in fork length, swimming steadily at $1.2\,FL\,s^{-1}$, where *FL* is fork length. Flow velocity is represented by black vectors plotted over a color background indicating vorticity. (A) Only low levels of vorticity (green) are present in the horizontal plane of fluid just above the caudal fin, as seen when the dorsal tip of the tail just intersects the sheet (indicated by the schematic view of the caudal fin relative to the light sheet to the left of each plot). Relatively strong negative and positive vorticity, associated with counterclockwise and clockwise vortices, respectively, and a broad central jet of flow are seen when the middle of the tail's upper lobe intersects the light sheet (B) and when the light sheet is at the lateral midline of the tail (C). One vortex ring is shed during each stroke of the caudal fin.

vortices were symmetrical at 1.2 *FL* s^{-1}. Vortex circulation and momentum were also independent of individual (P=0.087 and P=0.130, respectively; Table 2) and the interaction effect of individual×light-sheet orientation (P=0.593 and P=0.559, respectively, Table 2). Vortex circulation and momentum values determined from the horizontal light-sheet data were approximately twice the magnitude of those determined from the vertical light-sheet data (Table 1) because the strong lateral flow visible with the horizontal sheet (see, for example, Figs 2 and 3) was out of the plane of the vertical light sheet and was thus not viewed in the vertical light-sheet images. Despite these differences, the effect of light-sheet orientation was not statistically significant for vortex circulation or momentum (P=0.018 and P=0.019, respectively, Table 2) because a low P value was used to determine significance in order to correct for multiple comparisons.

The distance between vortex centers was independent of individual (P=0.043, Table 2) and the interaction of individual×light-sheet orientation (P=0.029, Table 2). Although the effect of light-sheet orientation on the distance between vortex centers was not statistically significant (P=0.033), ring width was on average 1.7 times ring height at the speed of 1.2 *FL* s^{-1} (Table 1), suggesting that the rings were elliptical instead of circular. This ratio increased to 1.9 at a speed of 2.2 *FL* s^{-1} (Table 1), indicating that the long axis of the ellipse increased in length with increased speed.

Ring axis angle relative to the X axis was independent of the effects of individual and individual×light-sheet orientation (P=0.013 and 0.367, respectively; Table 2). Light-sheet orientation had a significant effect on ring axis angle (P=0.006, Table 2). Jet angle to the X axis was also independent of the effects of individual and individual×light-sheet orientation (P=0.689 and P=0.413, respectively, Table 2), but was dependent on light-sheet orientation (P=0.001, Table 2). The dependence of these variables on light-sheet orientation reflects the fact that the vertical and horizontal light sheets showed perpendicular views of the obliquely oriented vortex rings.

Wake views obtained using the vertical light sheet (Fig. 4) suggested that the vertical ring axis was approximately perpendicular to the X axis. Values of ring axis angle to the X axis were close to 90 ° for both speeds (Table 1) although a range of values were seen, with some rings tilted by up to 30 ° from vertical (Fig. 6). Vertical light-sheet views of the wake also suggested that the angle of the jet to the X axis was nearly zero. Overall, jets were angled slightly negative to the X axis at both speeds (Table 1). The mean value of body angle at the swimming speed of 1.2 *FL* s^{-1} (–3±4 °, mean ± S.D., N=20, Table 1) was significantly different from zero (t-test, P=0.02). In the vertical plane, jet angle was independent of ring axis angle at the speed of 1.2 *FL* s^{-1} because the slope of a linear regression model fitted to the data was not significantly different from zero (ANOVA, P=0.57; Fig. 6). Jet angles at the speed of 2.2 *FL* s^{-1} showed a similar range and relationship to ring axis angle to those at the lower speed (Fig. 6).

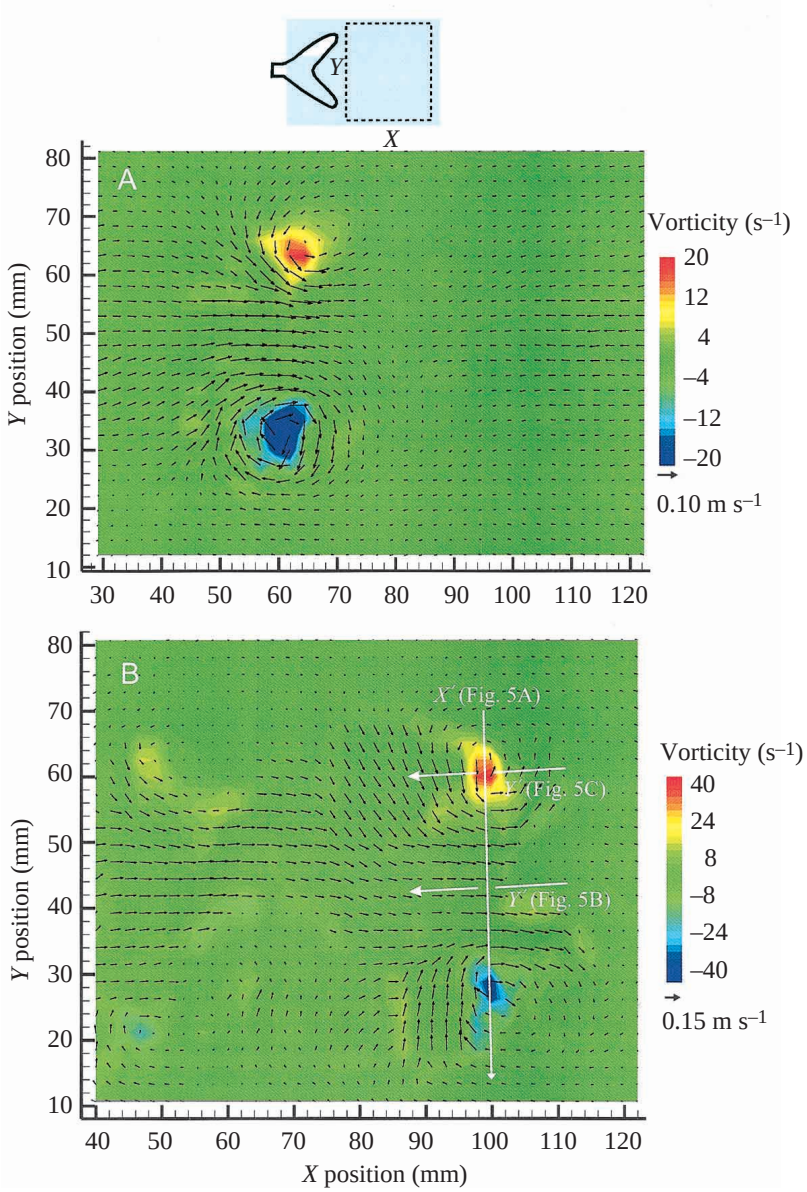

Fig. 4. Views of the wake in the vertical (*XY*) plane of an individual of *Scomber japonicus* 26 cm in fork length swimming steadily at speeds of 1.2 *FL* s^{-1} (A) and 2.2 *FL* s^{-1}, where *FL* is fork length (B). The orientation of the caudal fin to the light sheet is shown in the diagram. Flow velocity is represented by black vectors plotted over a color background indicating vorticity. At both swimming speeds, the caudal fin sheds one pair of counter-rotating vortices with a central jet of high-velocity flow per stroke. The white arrows and labels in B illustrate the axes of velocity profiles presented in Fig. 5. X' is the longitudinal axis of the ring; Y' is perpendicular to X'.

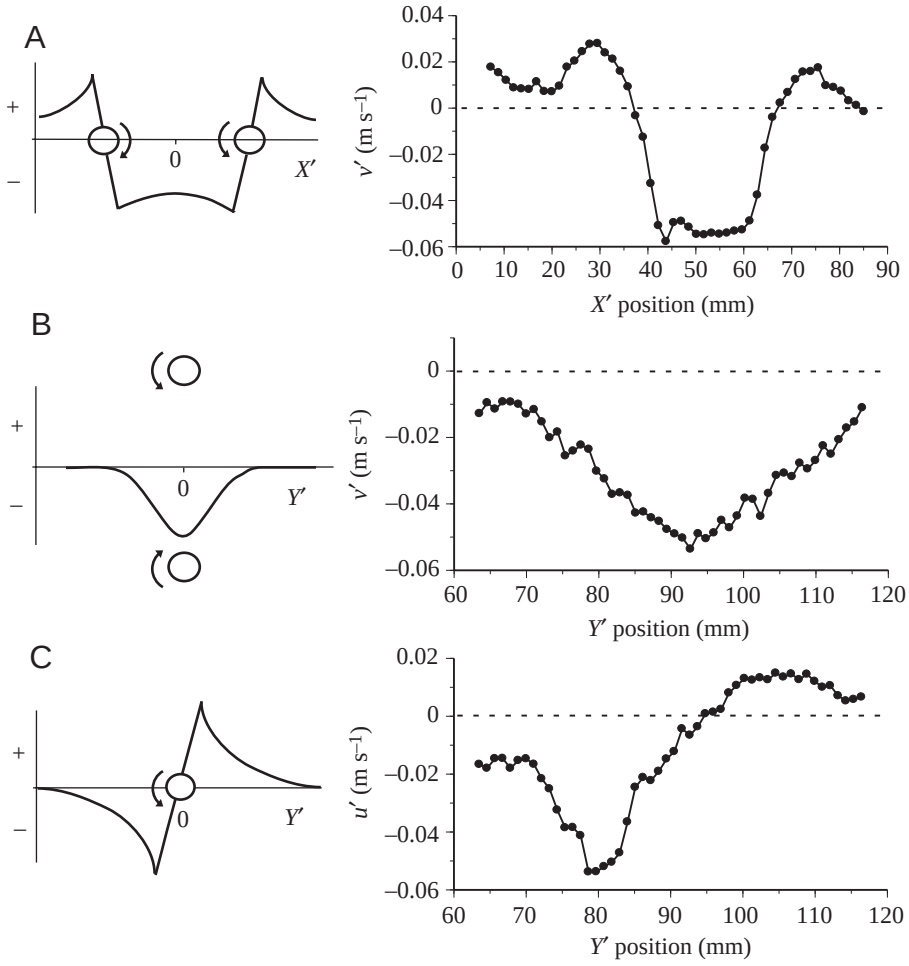

Fig. 5. Comparison of theoretically predicted velocity profiles across planar sections of isolated vortex rings (left panels, where paired circles indicate vortex cores in solid-body rotation and arrows indicate the direction of induced flow rotation; Milne-Thompson, 1966) with velocity profiles taken from *XY* planar light-sheet images of the wake of a mackerel 26 cm (fork length, *FL*) swimming at 1.2 *FL* s^{-1} (right panels). The velocity values shown are raw data calculated using a high-resolution 50×50 vector field. (A) *X*′ is the longitudinal axis of the vortex ring, which traverses the centers of the two vortex cores; (B) *Y*′ is the central axis of a vortex ring (perpendicular to *X*′); (C) *Y*′ is the line extending across the counterclockwise vortex core parallel to the ring's central axis (see Fig. 4B for an illustration of axes used here on an *XY* planar vorticity plot). The components of velocity parallel to *X*′ and *Y*′ are *u*′ and *v*′, respectively. In the region of the central jet, *v*′ is negative.

Wake views obtained using the horizontal light sheet (e.g. Figs 2, 3) indicated that the ring axis was at an oblique angle to the horizontal and that the jet was approximately perpendicular to the ring axis angle. On average, values of ring axis angle to the *X* axis from the 40 rings analyzed were approximately 30 ° (Table 1). Values of jet angle relative to the *X* axis were always less than 90 ° and tended to be lower at the speed of 2.2 *FL* s^{-1} (Table 1; Fig. 6). In the horizontal plane, jet angle was independent of ring axis angle because the slope of a regression model fitted to the data was not significantly different from zero (ANOVA, P=0.22; Fig. 6).

As discussed above, *S. japonicus* tended to swim with a slightly negative body angle (Table 1). Body angles (determined at the time each vortex was shed) ranged from –10 to +2 ° (Fig. 7). Both ring angle and jet angle values were independent of body angle at 1.2 *FL* s^{-1} (Fig. 7) because the slopes of regression models fitted to the data were not significantly different from zero (ANOVA, P=0.08 for ring angle and P=0.61 for jet angle). The data were similar at 2.2 *FL* s^{-1}.

Force magnitudes and balance

Three factors determine the magnitude of force produced (equation 1): stroke duration, vortex area and vortex circulation. Jet angle in the horizontal plane determines the ratio of thrust to lateral force produced. As discussed above, mean values of vortex area and stroke duration and individual values of vortex circulation, momentum and jet angle were used to calculate force. Estimates of downstream force were independent of individual (P=0.172; Table 2), light-sheet

Table 2. *Results (*F*-values) of ANOVAs on wake parameters at a steady swimming speed of 1.2* FL s^{-1}

Variable	Individual	Light-sheet orientation	Individual × light-sheet orientation
Degrees of freedom	4, 32	1, 2	2, 1
Distance between vortex centers	2.8	28.5	4.0
Ring axis angle	3.8	173.2*	1.0
Jet angle	0.6	700*	0.9
Vortex radius	0.8	1.2	0.7
Vortex circulation	2.2	55.8	0.5
Vortex momentum	1.9	50.5	0.6
Downstream force	1.7	7.8	0.3

*Statistically significant effect (P<0.007). Significant P value calculated to correct for multiple tests performed (Rice, 1989).

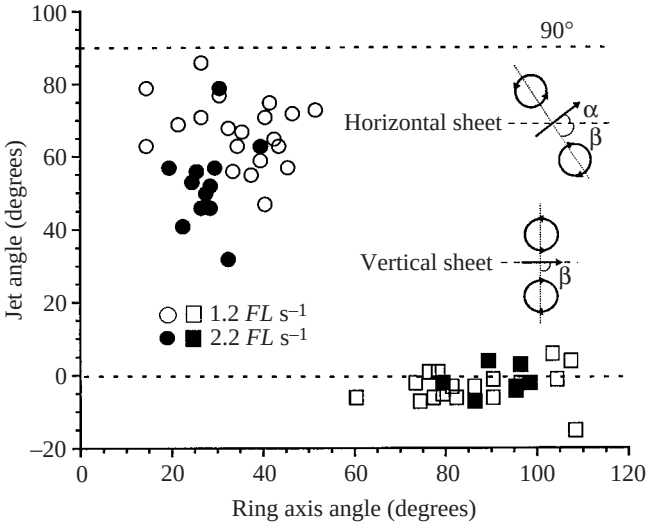

Fig. 6. Jet angle as a function of ring axis angle. Diagrams indicate jet (α) and ring axis (β) angle relative to the *X* axis as defined for vortices viewed with a horizontal (top diagram) and a vertical (bottom diagram) light sheet. Note that α is not shown in the vertical sheet diagram because jet angle relative to the *X* axis is 0°. Viewed in the *XZ* plane (horizontal light-sheet data, circles) at 1.2 *FL* s^{-1} (open symbols) or 2.2 *FL* s^{-1} (filled symbols), the angle of the jet flow to the *X* axis was always less than 90° (upper dotted line), indicating a thrust component to the jet. Viewed in the *XY* plane (vertical light-sheet data, squares), jet orientation was typically slightly negative relative to the *X* axis (lower dotted line) over a range of ring axis angles of more than 40°. *FL*, fork length.

orientation (P=0.107; Table 2) and the interaction effect of individual×light-sheet orientation (P=0.750; Table 2). Thus, there were no significant differences between estimates of downstream force from the separate measurements of force production made using the vertical and horizontal light sheets.

At the swimming speed of 1.2 *FL* s^{-1}, the magnitude of mean downstream force was 11±6 mN (mean ± S.D., N=40). Lateral forces, calculated from horizontal light-sheet data, were independent of individual (ANOVA, F=1.577, P=0.234) and high in magnitude (22±6 mN, mean ± S.D., N=20). Vertical forces (calculated from vertical light-sheet data) were also independent of individual (ANOVA, F=1.975, P=0.158) and were low in magnitude (–1±1 mN, mean ± S.D., N=20; Table 1). Thus, lateral forces dominated the wake, resulting in a mean mechanical performance (η, equal to thrust/total force) of 0.32 at 1.2 *FL* s^{-1}.

At the swimming speed of 2.2 *FL* s^{-1}, downstream forces calculated from the vertical (N=7) and horizontal (N=12) light-sheet images were not significantly different (ANOVA, F=0.494, P=0.491). At the speed of 2.2 *FL* s^{-1}, downstream force magnitude was 48±16 mN (mean ± S.D., N=19). Thus, on average, an increase in speed by a factor of 1.8 resulted in an increase in downstream force by a factor of 4.4. Mean lateral force at 2.2 *FL* s^{-1} increased by a factor of 3.0 to 65±14 mN (mean ± S.D., N=12). Mean vertical forces of –1±2 mN (mean ± S.D., N=7) at 2.2 *FL* s^{-1} were essentially identical to those seen at the lower speed. On average, η increased to 0.42 at 2.2 *FL* s^{-1}.

Measurements of drag made using a force transducer with the two smallest fish used in the DPIV experiments (*post mortem*) indicated that at the speed of 1.2 *FL* s^{-1} total drag was 9±0 mN (mean ± S.D., N=3) for the 20 cm fish and 11±1 mN (mean ± S.D., N=3) for the 22 cm fish. In comparison, thrust estimates made using DPIV analysis were 9±3 mN (mean ± S.D., N=5) for the 20 cm fish and 14±7 mN (mean ± S.D., N=5) for the 22 cm fish. In both cases, estimates of drag using the transducer and DPIV analysis were not significantly different based on a comparison of median values using the Kruskal–Wallis test (P=0.18 for the 20 cm fish and P=0.35 for 22 cm fish).

Discussion

The present flow visualization data, including flow patterns visualized with both the horizontal and vertical light sheets and the agreement between theoretical velocity profiles for vortex rings and the velocity profiles of the wakes analyzed here, indicate that during caudal fin locomotion *Scomber japonicus* produces linked ring vortices, each with a downstream-directed central jet. Fig. 8 is a schematic depiction of the wake of *S. japonicus* summarizing our major numerical findings of wake geometry and DPIV estimates of locomotor forces.

This pattern of flow is termed a reverse von Kármán (or thrust) wake (von Kármán and Burgers, 1935; Lighthill, 1975); it is produced by an oscillating, thrust-producing foil moving steadily forwards (Triantafyllou et al., 1991, 1993, 2000;

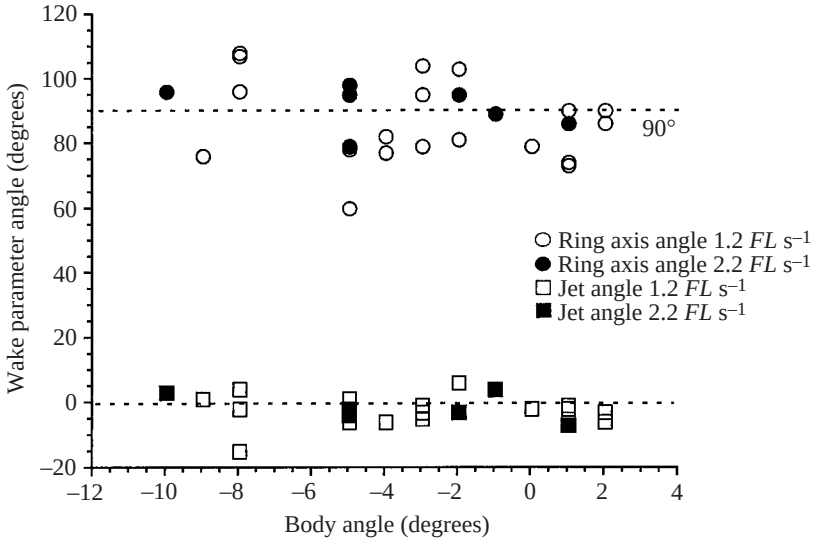

Fig. 7. Ring axis angle (circles) and jet angle (squares) relative to body angle to the *X* axis at swimming speeds of 1.2 *FL* s^{-1} (open symbols) and 2.2 *FL* s^{-1} (filled symbols). All measurements were made in the vertical (*XY*) plane. *FL*, fork length.

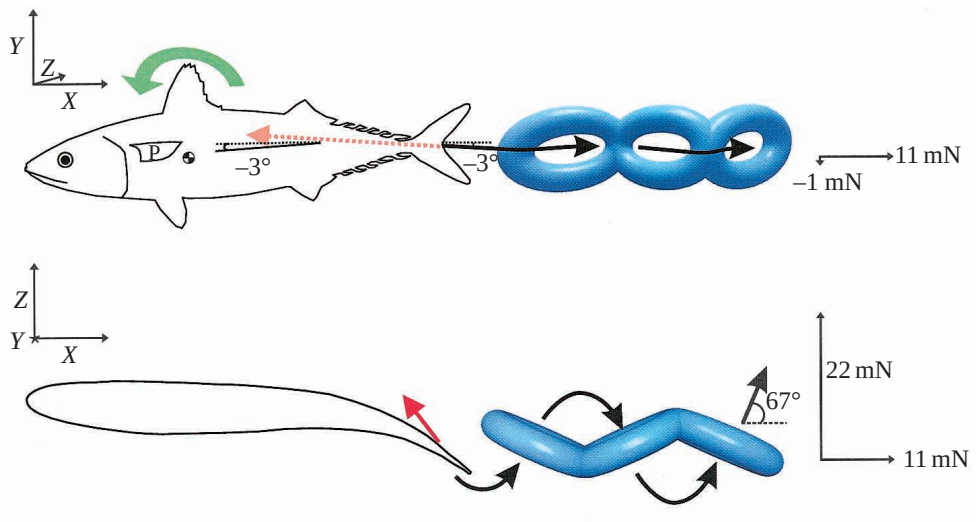

Fig. 8. Summary of the empirically determined hydrodynamic forces created by chub mackerel *Scomber japonicus* swimming steadily at 1.2 *FL* s^{-1}. Flow fields and forces are depicted in the vertical (*XY*, top) and horizontal (*XZ*, bottom) planes. Vortex rings are shown in blue; ring dimensions and orientation represent those determined empirically in this paper (Table 1). Thick black arrows represent central jet flow. Red arrows represent the reaction force on the caudal fin; in the vertical plane, reaction force is directed behind the body, so the red arrow is broken. Thrust, lift and lateral force values are the mean reaction forces averaged over a stroke period. *S. japonicus* swims with its body slightly tilted down (–3 ° on average); the jet is tilted down –3 ° in the opposite direction. Thus, the reaction force at the caudal fin has a lift component that acts over the lever arm of body length to the center of mass (black-and-white checkered circle) to rotate the head down (green arrow). Lift generated by abducted pectoral fins (P), such as has been observed in previous kinematic studies, could counterbalance lift generated at the caudal fin.

Anderson, 1996; Anderson et al., 1998). Reverse von Kármán wakes are produced during caudal fin locomotion by bluegill sunfish *Lepomis macrochirus* (Lauder, 2000; Drucker and Lauder, 2001b), giant danio *Danio malabaricus* (Anderson, 1996; Wolfgang et al., 1999), mullet *Chelon labrosus* (Müller et al., 1997; Videler et al., 1999), trout *Oncorhynchus mykiss* (Blickhan et al., 1992) and white sturgeon *Acipenser transmontanus* (Liao and Lauder, 2000). The wake morphology of a double row of pairs of vortices, reported for caudal fin locomotion by eel *Anguilla anguilla* (Müller et al., 2001) and danio *Brachydanio albolineatus* (Rosen, 1959), was not created by *S. japonicus*. In addition, the wake of a single large vortex ring modeled for caudal fin locomotion by eel (Carling et al., 1998) and the model of ‘wakeless’ caudal fin locomotion due to the sequential creation and destruction of vortices modeled for a forked caudal fin by Ahlborn et al. (1991) were not supported by the present data. The timing of vortex shedding during the first quarter of each stroke in *S. japonicus* is similar to that described for the danio *Brachydanio rerio* (McCutchen, 1976) and the giant danio (Wolfgang et al., 1999).

Vortex geometry

Vortex ring height was approximately equal to caudal fin height, indicating that caudal fin size determines one parameter of vortex size (as noted by Blickhan et al., 1992; Müller et al., 2000). The magnitude of caudal fin excursion in the *Z* dimension determined the distance between the vortices in the *XZ* plane and, thus, the length of the vortex ring. These data suggest that the vortex rings were elliptical rather than round in shape (Fig. 8), as was inferred for the vortex rings in the wake of the mullet *Chelon labrosus* (Müller et al., 1997). As the length of the ellipsoid was dependent on speed and was approximately double the height of the ellipse at the speed of 2.2 *FL* s^{-1}, the data indicate that accurate measurements of ring geometry (which are necessary for force calculations) require measurements of vortex ring geometry in both the *XY* and *XZ* planes.

The elliptical shape of the vortex rings seen here is a departure from the axisymmetrical shape of an ideal vortex ring (according to Helmholtz’s theorem; see Milne-Thompson, 1966). A second departure of the present data from the characteristics of an ideal vortex ring is seen in the geometric relationship between the vertical ring axis and the central jet. The central jet flow of an ideal vortex ring (such as that created by ejection of fluid from a circular nozzle by a piston, see Webster and Longmire, 1997; Raffel et al., 1998) extends perpendicular to the plane of the vortex ring. In the wake of *Scomber japonicus*, however, the angle of the jet to the *X* axis was typically close to 0 °, although the ring axis angle to the *X* axis varied from 60 to 110 ° (with 90 ° being vertical). Variability in the angle between the vertical ring axis and the central jet has been seen in wakes created during pectoral fin locomotion by bluegill sunfish *Lepomis macrochirus* (Drucker and Lauder, 1999) and during caudal fin locomotion by sturgeon *Acipenser transmontanus* (Liao and Lauder, 2000) and *L. macrochirus* (Lauder, 2000). The described differences between the wake structures seen here and those of ideal vortex rings have been attributed to the fact that these wakes are produced by reciprocating hydrofoils that are flexible, deform in a complex manner under load and are undergoing unsteady motions [see, for example, bluegill pectoral fin kinematics (Gibb et al., 1994) and mackerel caudal fin kinematics (Gibb et al., 1999)]. Given the differences in shape and jet orientation between ideal vortex rings and the wake described here, the wake of *Scomber japonicus* may be most appropriately described as a series of linked vortex ‘loops’ rather than rings (Dickinson and Götz, 1996).

Force magnitudes and balance

Estimates of thrust calculated from separate DPIV measurements in the vertical and horizontal planes were not significantly different. In addition, for the two smallest animals that could be tested (20 and 22 cm fork length), there was no significant difference between estimates of thrust based on DPIV measurements and measurements of total body drag obtained by towing those animals at the same flow speed.

Note that the present force data based on DPIV measurements were calculated using the full values of vortex circulation obtained for both the horizontal and vertical planes. In the only previous study of caudal fin locomotion in which forces were calculated from DPIV data and compared with independent force estimates (in that case, force estimates calculated from a kinematic model; Müller et al., 1997), wake vortices were visualized in the horizontal plane only, and the value of half the measured circulation was used to calculate fluid forces on the basis of the premise that the vortices viewed in the horizontal plane are linked and that the circulation visible in that plane is equivalent to the added circulation of two rings. In the present study, the magnitude of vortex circulation viewed using the horizontal light sheet was approximately twice that of the vortices viewed using the vertical light sheet (Table 1) because the vertical light sheet showed fluid movement in the vertical plane only and thus missed the strong lateral flow component. The full value of vortex circulation was used here to calculate forces from data collected in both planes, and the good agreement between present estimates of thrust from the vertical and horizontal light-sheet data together with the lack of significant difference between the thrust estimates and the drag measurements support this methodology and the force balance presented in Fig. 8.

A balance between thrust and drag is predicted for an animal moving at a steady speed; however, such force balances have been difficult to demonstrate empirically. The present study demonstrates such a balance with the lack of significant difference between drag measurements obtained by towing dead animals and thrust estimates obtained from DPIV measurements by the same animals swimming freely at the same speed. For one animal, the measured body drag measurements were lower (although not significantly so) than the thrust estimates, which may be attributable to the fact that oscillation of the caudal peduncle and fin by a swimming fish will increase its drag (Webb, 1975). Drag is proportional to the square of velocity, so one would predict increases in drag by a factor of 3.4 as swimming speed increased from 1.2 to 2.2 $FL\,s^{-1}$ (assuming no change in drag due to transitions from laminar to turbulent flow in the boundary layer). On the basis of the DPIV measurements, thrust increased, on average, by a factor of 4.4.

Measurements of whole-body drag in fishes are notoriously difficult to perform, and a host of experimental and theoretical issues potentially confound estimates of whole-body drag (for reviews, see Webb, 1975; Dickinson, 1996). We also experienced considerable difficulty in obtaining repeatable measurements of whole-body drag, and our estimates do not take into account changes in drag that might result from locomotor movements. Nonetheless, the general quantitative agreement obtained here between estimates of thrust from DPIV and drag obtained from towing fish at the same speed suggests that the DPIV force estimates are at least reasonable estimates of the thrust needed to overcome drag at the swimming speeds studied. Indeed, given recent advances in DPIV methodology, DPIV measurements are in some ways more reliable and repeatable than data obtained from towing fish. One possible objection to the DPIV approach is that during caudal fin locomotion momentum is removed from fluid passing over the body. This same fluid is then reaccelerated by the caudal fin, making it difficult to determine the total momentum added to the fluid and, thus, absolute values of thrust. While this is a valid theoretical issue, in practice, the mackerel caudal fin encounters nearly free-stream flow (Nauen and Lauder, 2000a) because of its lateral oscillation and the vertical extent of the fin well above and below the caudal peduncle. This suggests that the caudal-fin-generated vortex rings in mackerel measured here probably capture the majority of momentum imparted to the water by the mackerel and, hence, that the present measurements reflect the thrust needed to overcome drag during steady swimming.

The thrust of the order of 11 mN determined here for caudal fin locomotion by *Scomber japonicus* at 1.2 $FL\,s^{-1}$ (Table 1) is approximately a quarter of the 40 mN produced by both pectoral fins of bluegill sunfish, *Lepomis macrochirus*, of slightly smaller size (approximately 20 cm *TL*) swimming at 1 $TL\,s^{-1}$ (Drucker and Lauder, 1999) but similar to the mean thrust force of 14 mN produced by the caudal fin of *L. macrochirus* (approximately 21 cm *TL*) swimming at 1.1 $FL\,s^{-1}$ (Drucker and Lauder, 2001b, p. 2949). At 1.1 $TL\,s^{-1}$, *L. macrochirus* also uses its dorsal fin and pectoral fins to swim, however, so that the total thrust produced by a bluegill (56 mN) is approximately five times that of *S. japonicus* at a similar speed. The large discrepancy in thrust force magnitudes produced by the two species at the relatively slow cruising speed of approximately 1 $TL\,s^{-1}$ probably reflects the high drag of the relatively deep and globose body of *L. macrochirus* compared with the streamlined body of *S. japonicus*.

Force production

Vortex central jet flow orientation relative to the fish's path of motion determines the proportion of the total reaction force that is thrust and, thus, the mechanical performance (η) of the stroke. A jet oriented opposite to the direction of travel of the fish generates a reaction force composed completely of thrust, with η values of 1. Jets oriented at an angle to the direction of travel result in a reaction force that is a combination of thrust and lateral forces. It has been predicted that the wake of a well-streamlined fish (such as a scombrid) swimming steadily forwards without accelerating would produce only a weak 'thrust' wake without strong lateral flows that may be difficult to visualize (Rayner, 1995). The wakes generated by *Scomber japonicus* were easily visualized, however, and contained

lateral flows up to approximately twice the magnitude of downstream flows, so that values of η (0.32 at the swimming speed of 1.2 *FL* s^{-1} and 0.42 at the swimming speed of 2.2 *FL* s^{-1}) were relatively low.

The high magnitude of lateral forces seen here was somewhat surprising given that the chub mackerel *Scomber japonicus* is a member of the family Scombridae, a family of fish that includes bonitos and tunas. These fishes are noted for high-performance locomotion in terms of high burst speeds [from 18 *TL* s^{-1} for mackerel (Wardle and He, 1988) to up to 27 *TL* s^{-1} for tuna (Fierstine and Walters, 1968; see also Magnuson, 1978)], high cruising speeds (3.5 to greater than 5 *TL* s^{-1} for mackerel, Wardle and He, 1988; Sepulveda and Dickson, 2000) and 6–10 *TL* s^{-1} for tuna (Yuen, 1970; summarized in Beamish, 1978) and long migration distances (as far as 9700 km for the trans-Pacific crossing of the bluefin tuna; Lindsey, 1978). Morphological adaptations thought to increase locomotor performance include a streamlined body that tapers to a caudal peduncle with finlets and a forked (mackerel), semi-lunate (bonito) or lunate (tuna) caudal fin shape.

The suite of morphological characters described above forms the basis of the prediction that scombrid fish would generate only a weak 'thrust' wake of high efficiency (Rayner, 1995). In addition, the data cited above suggest that more derived members of the scombrid clade show greater locomotory performance. Specific differences in steady swimming kinematics have been identified between juvenile kawakawa tuna (*Euthynnus affinis*) and juvenile *S. japonicus* (Donley and Dickson, 2000). At a given steady swimming speed, *E. affinis* shows significantly less lateral body displacement than *S. japonicus* (Donley and Dickson, 2000); such decreased axial flexion is characteristic of thunniform locomotion and has been previously documented for tunas (Fierstine and Walters, 1968; Dewar and Graham, 1994). However, lateral movement at the tip of the snout, or yaw (which contributes to drag), was not significantly different between the two species, and *E. affinis* showed higher tailbeat frequencies than *S. japonicus* at the same swimming speeds (Donley and Dickson, 2000).

More direct measurements of locomotor performance also indicate surprisingly little difference between juvenile tuna and mackerel. Sepulveda and Dickson (2000) determined that maximum sustainable speeds and net cost of transport (and therefore swimming efficiency) are not significantly different between juvenile *E. affinis* and juvenile *S. japonicus*. Thus, detailed studies of swimming kinematics (Donley and Dickson, 2000) and cost of transport (Sepulveda and Dickson, 2000) indicate that juvenile tuna are not more efficient propulsors than mackerel of the same size.

On the basis of the previous kinematic and physiological data, we predict that the wake flow patterns and thrust and drag measurements made here are generally applicable to more derived scombrid species of similar size swimming at the speeds studied here. Note that this comparison is facilitated by the fact that mean tailbeat frequencies seen here for *Scomber japonicus*, 2.5 Hz and 4.2 Hz at swimming speeds of 1.2 and 2.2 *FL* s^{-1}, respectively, are similar to the values of 2.9 Hz and 4.0 Hz seen previously (tailbeat frequencies calculated for those speeds from Table 1 of Donley and Dickson, 2000). Mean tailbeat frequencies for *S. japonicus* of Gibb et al. (1999) were very similar at 1.2 *TL* s^{-1} (2.4 Hz) but lower (3.0 Hz) at 2.2 *TL* s^{-1} than those measured here.

The present data also indicate a surprising lack of difference in mechanical performance between a scombrid and a more basal perciform fish, the bluegill sunfish *Lepomis macrochirus*. Mean mechanical performance for *Scomber japonicus* swimming steadily at 1.2 *FL* s^{-1} is 0.32, which is slightly less than the η values of 0.39 for labriform swimming by the bluegill sunfish *Lepomis macrochirus* (Drucker and Lauder, 1999) and 0.38 for caudal fin locomotion by *Lepomis macrochirus* (Drucker and Lauder, 2001b) for similarly sized fish swimming at nearly identical speeds. Note that all the previous η values are much lower than the value of 0.7 calculated for trout (Blickhan et al., 1992) and the value of 0.97 calculated for the mullet (Müller et al., 1997), although few specifics of those data are available for direct comparison. The similarity of mechanical performance of caudal fin locomotion for fishes as disparate in morphology and locomotor habit as chub mackerel and bluegill suggests that undulatory carangiform propulsion in fishes with homocercal tails is relatively inefficient from a mechanical perspective.

A different measure of the caudal fin performance is the Strouhal number (*St*):

$$St = fWU^{-1}, \quad (2)$$

where *f* is tailbeat frequency, *W* is wake width (estimated here from tailbeat amplitude) and *U* is swimming velocity. *St* values within the range 0.25–0.35 indicate that the caudal fin is oscillating at optimal performance (i.e. maximum thrust per unit input energy; Triantafyllou et al., 1993) and producing a wake with a strong thrust force (see Fig. 17 in Anderson et al., 1998). Such wakes were visualized in the present study. On the basis of the detailed caudal fin kinematic data of Gibb et al. (1999) for similarly sized individuals of *Scomber japonicus* (24.8 cm mean *TL versus* 23 cm mean *FL* in the present study) swimming in the flow tank used here at the same relative speeds studied here, *S. japonicus* operates at *St* values of 0.30 at speeds of 1.2 *FL* s^{-1} and at *St* values of 0.26 at speeds of 2.2 *FL* s^{-1}. Both these *St* values are within the range of values indicating high performance, despite the production of high lateral forces seen here.

The present data indicate that high lateral force production is a feature of caudal fin locomotion by chub mackerel. Combined with the study of Drucker and Lauder (2001b), it appears that high lateral forces and relatively low mechanical performance are a general feature of caudal fin locomotion by teleost fishes at speeds of approximately 1 *FL* s^{-1} and not a limitation of pectoral fin locomotion or of fishes with relatively low locomotor capacity (such as bluegill sunfish). Low mechanical performance for caudal fin locomotion might reflect the nature of undulatory propulsion as a posteriorly

propagated wave of lateral bending, which may necessitate the generation of relatively large lateral forces. Supporting this hypothesis is the finding of Triantafyllou et al. (1991) of optimum mechanical performance values of approximately 0.2 at Strouhal numbers of 0.2–0.3 for foils oscillating transversely through uniform oncoming flow. Such foils are physical models of caudal fin locomotion at a steady forward speed.

Lift production by a homocercal tail

A second feature of vortex jet orientation important to force production is the orientation of the jet relative to the *X* axis (defined in Fig. 1). An orientation of 0 ° indicates that the jet is horizontal and that the caudal fin is not producing lift. Lift is an important factor in the force balance of animals moving through water as it is necessary for maneuverability and to counteract negative buoyancy. Lift may be produced by the interaction between virtually any fin or body surface and the fluid. For example, on the basis of a kinematic study of body angle as a function of swimming speed for the Atlantic mackerel *Scomber scombrus*, He and Wardle (1986) suggested that negatively buoyant fishes produce lift by swimming at a positive body angle. Hydrodynamic evidence of such lift production during steady swimming has been provided for leopard shark *Triakis semifasciata* (Wilga and Lauder, 2000) and white sturgeon *Acipenser transmontanus* (Wilga and Lauder, 1999). Lift production by the caudal fin has been demonstrated for *T. semifasciata* (Ferry and Lauder, 1996) and *A. transmontanus* (Liao and Lauder, 2000); lift production by pectoral fins has been demonstrated for bluegill sunfish *Lepomis macrochirus* (Drucker and Lauder, 1999, 2000) and black surfperch *Embiotoca jacksoni* (Drucker and Lauder, 2000).

The caudal fin of *Scomber japonicus* is externally symmetrical, or homocercal, in shape. Homocercal caudal fins are classically viewed as moving symmetrically in the lateral plane (as a homogeneous, stiff, flat plate) and generating only lateral forces and thrust but not lift (for a review, see Lauder, 2000). Recent kinematic data on the homocercal caudal fin of bluegill sunfish indicate, however, that the fin moves at an acute angle to the horizontal plane with asymmetrical movement of the fin's dorsal and ventral lobes that would generate lift (Lauder, 2000). This hypothesis was confirmed with DPIV analysis of the wake, which consisted of a chain of linked vortex rings with a jet of flow that was somewhat ventrally inclined (Lauder, 2000).

Analysis of caudal fin movement by *Scomber japonicus* (Aleev, 1969; Gibb et al., 1999) indicated that, like the bluegill sunfish, the homocercal caudal fin is at an acute angle relative to the vertical axis during lateral movement. On the basis of these kinematic data, one would predict that the caudal fin of *S. japonicus* generates lift that can be visualized as a ventrally oriented central jet of flow in each vortex ring. As predicted from the kinematic data, the vortex jet was oriented at a slightly negative angle relative to the *X* axis [–3 °, which is in the same direction but at a substantially smaller angle than that demonstrated for sharks (Ferry and Lauder, 1996) and sturgeon (Liao and Lauder, 2000)]. This posteroventral orientation resulted in the generation of small negative lift forces (approximately –1 mN).

S. japonicus swam with their bodies tilted slightly head-downward, however (on average, also 3 ° below horizontal), as has been found previously (Gibb et al., 1999). In comparison, their sister species *S. scombrus* tend to swim with a body angle of approximately 0 ° at their preferred swimming speeds of 0.9–1.2 *TL* s^{-1} (He and Wardle, 1986); *S. scombrus* tilts its head up and reaches body angles as high as 20 ° when swimming speeds decrease to 0.4–0.8 *TL* s^{-1} (He and Wardle, 1986). The slightly negative body angle of *S. japonicus* seen here resulted in a net 6 ° difference between the orientation of the body and the jet (Fig. 8). Reaction forces generated at the caudal fin would be oriented at +3 ° above the horizontal, thus generating a small but probably significant lift force tending to rotate the animal about its center of mass by inducing a torque.

Lift generated by orientation of the body or pectoral fins to oncoming flow could counteract lift generation at the caudal fin (Magnuson, 1973, 1978). The body orientation of *Scomber japonicus* probably does not generate high magnitudes of lift at the low orientation angles seen here and previously (Gibb et al., 1999). The pectoral fins, a prominent feature in the more derived scombrid species, are a second potential source of lift (Magnuson, 1970, 1978). The pectoral fins of *S. japonicus* are frequently abducted during steady swimming at the speeds studied here (Gibb et al., 1999), and any lift forces generated would act at the base of the fin, which is anterior to the center of mass (Fig. 8). To test this hypothesis would require visualization of the wake of *S. japonicus* pectoral fins, as has been performed for other fishes (Drucker and Lauder, 1999, 2000; Wilga and Lauder, 1999, 2000) and calculation of a whole-body vertical force balance.

The whole-body vertical force balance for *Scomber japonicus*, and for the genus *Scomber*, is complicated by morphological variation within the genus and among scombrids in general. Swimbladder presence and size are variable among scombrids and are not a diagnostic feature of the group (Collette, 1978). The swimbladder of *S. japonicus* in the size range studied here has an elongate oval shape; its center is positioned approximately at the center of mass of the animal (J. C. N. and G. V. L., personal observation). Thus, the swimbladder is unlikely to compensate for lift forces produced by the caudal fin. Of the remaining two *Scomber* species, *S. australasicus* also has a swimbladder, but the organ is lacking from *S. scombrus* (Collette and Nauen, 1983). With regard to the more derived scombrids, *Thunnus tonggol* also lacks a swimbladder (Collette, 1978), and other members of Thunnini have a swimbladder as juveniles, but the structure degenerates with growth (e.g. *Auxis* and *Euthynnus*; Richards and Dove, 1971).

Pectoral fin size, another potential factor in lift production, is also variable, although the relatively large pectoral fin surface area and the presence of a swimbladder are found more often in scombrid species of larger body size (Magnuson, 1973). Median bony caudal keels present on the caudal

peduncle of derived scombrids (but not externally on *S. japonicus*; Nauen and Lauder, 2000) have also been proposed as lift generators (Magnuson, 1970, 1978). Variability in the presence of a swimbladder and a central caudal keel, as well as changes in pectoral fin size and factors such as body fat content and distribution (and thus fish density) over ontogeny and among species, suggests that there will be considerable differences between the vertical force balances of different scombrid fishes swimming under different conditions. The scombrid homocercal caudal fin may show interesting differences in function under these variable conditions.

The authors thank Cheryl Wilga for assistance with obtaining mackerel for this study. We also thank Eliot Drucker, Laura Farrell, Ellen Freund, Tonia Hsieh, Jimmy Liao and Eric Tytell for helpful comments during the course of the study. Numerous conversations with Paul Webb greatly enhanced our understanding of issues surrounding drag and thrust measurements, and we very much appreciate his comments (although he may not agree with our conclusions). The suggestions of two anonymous reviewers improved the manuscript. Support was provided by NSF grant 9807021 to G.V.L.

References

Ahlborn, B., Harper, D. G., Blake, R. W. and Ahlborn, D. (1991). Fish without footprints. *J. Theor. Biol.* **148**, 521–533.

Aleev, Y. G. (1969). *Function and Gross Morphology in Fish*. Jerusalem: Keter Press.

Anderson, E. J., McGillis, W. R. and Grosenbaugh, M. A. (2000). The boundary layer of swimming fish. *J. Exp. Biol.* **204**, 81–102.

Anderson, J. M. (1996). Vorticity control for efficient propulsion. PhD thesis, Massachusetts Institute of Technology and the Woods Hole Oceanographic Institution.

Anderson, J. M., Streitlien, K., Barrett, D. S. and Triantafyllou, M. S. (1998). Oscillating foils of high propulsive efficiency. *J. Fluid Mech.* **360**, 41–72.

Batchelor, G. K. (1967). *An Introduction to Fluid Mechanics.* Cambridge: Cambridge University Press.

Beamish, F. W. H. (1978). Swimming capacity. In *Fish Physiology*, vol. VII, *Locomotion* (ed. W. S. Hoar and D. J. Randall), pp. 101–189. New York: Academic Press.

Blickhan, R., Krick, C., Zehren, D. and Nachtigall, W. (1992). Generation of a vortex chain in the wake of a subundulatory swimming. *Naturwissenschaften* **79**, 220–221.

Carling, J., Williams, T. L. and Bowtell, G. (1998). Self-propelled anguilliform swimming: simultaneous solution of the two-dimensional Navier–Stokes equations and Newton's laws of motion. *J. Exp. Biol.* **201**, 3143–3166.

Collette, B. B. (1978). Adaptations and systematics of mackerels and tunas. In *The Physiological Ecology of Tunas* (ed. G. D. Sharp and A. E. Dizon), pp. 7–39. New York: Academic Press.

Collette, B. B. and Nauen, C. E. (1983). *Scombrids of the World*. Rome: Food and Agriculture Organization of the United Nations.

Dewar, H. and Graham, J. B. (1994). Studies of tropical tuna swimming performance in a large water tunnel. III. Kinematics. *J. Exp. Biol.* **192**, 45–59.

Dickinson, M. H. (1996). Unsteady mechanisms of force generation in aquatic and aerial locomotion. *Am. Zool.* **36**, 537–554.

Dickinson, M. H. and Götz, K. G. (1996). The wake dynamics and flight forces of the fruit fly *Drosophila melanogaster*. *J. Exp. Biol.* **199**, 2085–2104.

Donley, J. M. and Dickson, K. A. (2000). Swimming kinematics of juvenile kawakawa tuna (*Euthynnus affinis*) and chub mackerel (*Scomber japonicus*). *J. Exp. Biol.* **203**, 3103–3116.

Drucker, E. G. and Lauder, G. V. (1999). Locomotor forces on a swimming fish: three-dimensional vortex wake dynamics quantified using digital particle image velocimetry. *J. Exp. Biol.* **202**, 2393–2412.

Drucker, E. G. and Lauder, G. V. (2000). A hydrodynamic analysis of fish swimming speed: wake structure and locomotory force in slow and fast labriform swimmers. *J. Exp. Biol.* **203**, 2379–2393.

Drucker, E. G. and Lauder, G. V. (2001a). Wake dynamics and fluid forces of turning maneuvers in sunfish. *J. Exp. Biol.* **204**, 431–442.

Drucker, E. G. and Lauder, G. V. (2001b). Locomotor function of the dorsal fin in teleost fishes: experimental analysis of wake forces in sunfish. *J. Exp. Biol.* **204**, 2943–2958.

Ferry, L. A. and Lauder, G. V. (1996). Heterocercal tail function in leopard sharks: a three-dimensional kinematic analysis of two models. *J. Exp. Biol.* **199**, 2253–2268.

Fierstine, H. L. and Walters, V. (1968). Studies in locomotion and anatomy of scombroid fishes. *Mem. S. Calif. Acad. Sci.* **6**, 1–31.

Gibb, A. C., Dickson, K. A. and Lauder, G. V. (1999). Tail kinematics of the chub mackerel *Scomber japonicus*: testing the homocercal tail model of fish propulsion. *J. Exp. Biol.* **202**, 2433–2447.

Gibb, A. C., Jayne, B. C. and Lauder, G. V. (1994). Kinematics of pectoral fin locomotion in the bluegill sunfish *Lepomis macrochirus*. *J. Exp. Biol.* **189**, 133–161.

Gillis, G. B. (1998). Environmental effects on undulatory locomotion in the American eel *Anguilla rostrata*: kinematics in water and on land. *J. Exp. Biol.* **201**, 949–961.

Hanke, W., Brucker, C. and Bleckmann, H. (2000). The ageing of the low-frequency water disturbances caused by swimming goldfish and its possible relevance to prey detection. *J. Exp. Biol.* **203**, 1193–1200.

He, P. and Wardle, C. S. (1986). Tilting behavior of the Atlantic mackerel, *Scomber scombrus*, at low swimming speeds. *J. Fish Biol.* **29**, 223–232.

Jayne, B. C., Lozada, A. F. and Lauder, G. V. (1996). Function of the dorsal fin in bluegill sunfish: motor patterns during four distinct locomotor behaviors. *J. Morphol.* **228**, 307–326.

Lauder, G. V. (2000). Function of the caudal fin during locomotion in fishes: kinematics, flow visualization and evolutionary patterns. *Am. Zool.* **40**, 101–122.

Liao, J. and Lauder, G. V. (2000). Function of the heterocercal tail in white sturgeon: flow visualization during steady swimming and vertical maneuvering. *J. Exp. Biol.* **203**, 3585–3594.

Lighthill, M. J. (1975). *Mathematical Biofluiddynamics*. Philadelphia: Society for Industrial and Applied Mathematics.

Lindsey, C. C. (1978). Form, function and locomotory habits in fish. In *Fish Physiology*, vol. VII, *Locomotion* (ed. W. S. Hoar and D. J. Randall), pp. 1–100. New York: Academic Press.

Magnuson, J. J. (1970). Hydrostatic equilibrium of *Euthynnus affinis*, a pelagic teleost without a gas bladder. *Copeia* **1**, 56–85.

Magnuson, J. J. (1973). Comparative study of adaptations for continuous swimming and hydrostatic equilibrium of scombrid and xiphoid fishes. *Fish. Bull.* **71**, 337–356.

Magnuson, J. J. (1978). Locomotion by scombrid fishes: hydromechanics, morphology and behavior. In *Fish Physiology*, vol. VII, *Locomotion* (ed. W. S. Hoar and D. J. Randall), pp. 239–313. New York: Academic Press.

McCutchen, C. W. (1976). Flow visualization with stereo shadowgraphs of stratified flow. *J. Exp. Biol.* **65**, 11–20.

Milne-Thompson, L. M. (1966). *Theoretical Aerodynamics*. New York: Macmillan.

Müller, U. K., Smit, J., Stamhuis, L. J. and Videler, J. J. (2001). How the body contributes to the wake in undulatory fish swimming: flow fields of a swimming eel (*Anguilla anguilla*). *J. Exp. Biol.* **204**, 2751–2762.

Müller, U. K., Stamhuis, E. J. and Videler, J. J. (2000). Hydrodynamics of unsteady fish swimming and the effects of body size: comparing the flow fields of fish larvae and adults. *J. Exp. Biol.* **203**, 193–206.

Müller, U. K., Van Den Heuvel, B. L. E., Stamhuis, E. J. and Videler, J. J. (1997). Fish foot prints: morphology and energetics of the wake behind a continuously swimming mullet (*Chelon labrosus* Risso). *J. Exp. Biol.* **200**, 2893–2906.

Nauen, J. C. and Lauder, G. V. (2000). Locomotion in scombrid fishes: morphology and kinematics of the finlets of the chub mackerel *Scomber japonicus*. *J. Exp. Biol.* **203**, 2247–2259.

Nauen, J. C. and Lauder, G. V. (2001a). Locomotion in scombrid fishes: visualization of flow around the caudal peduncle and finlets of the chub mackerel *Scomber japonicus*. *J. Exp. Biol.* **204**, 2251–2263.

Nauen, J. C. and Lauder, G. V. (2001b). A three-dimensional analysis of finlet kinematics in the chub mackerel (*Scomber japonicus*). *Biol. Bull.* **200**, 9–19.

Raffel, M., Willert, C. and Kompenhans, J. (1998). *Particle Image Velocimetry: A Practical Guide*. New York: Springer.

Rayner, J. M. (1995). Dynamics of the vortex wakes of flying and swimming vertebrates. In *Biological Fluid Dynamics* (ed. C. P. Ellington and T. J. Pedley), pp. 131–155. Cambridge: Company of Biologists Ltd.

Rice, W. R. (1989). Analyzing tables of statistical tests. *Evolution* **43**, 223–225.

Richards, W. J. and Dove, G. R. (1971). Internal development of young tunas of the genera *Katsuwonus*, *Euthynnus*, *Auxis* and *Thunnus* (Pisces, Scombridae). *Copeia* **1971**, 72–78.

Rosen, M. W. (1959). *Water Flow about a Swimming Fish*. China Lake, CA: United States Naval Ordinance Test Station.

Sepulveda, C. and Dickson, K. A. (2000). Maximum sustainable speeds and cost of swimming in juvenile kawakawa tuna (*Euthynnus affinis*) and chub mackerel (*Scomber japonicus*). *J. Exp. Biol.* **203**, 3089–3101.

Stamhuis, E. J. and Videler, J. J. (1995). Quantitative flow analysis around aquatic animals using laser sheet particle image velocimetry. *J. Exp. Biol.* **198**, 283–294.

Triantafyllou, G. S., Triantafyllou, M. S. and Grosenbaugh, M. A. (1993). Optimal thrust development in oscillating foils with application to fish propulsion. *J. Fluids Struct.* **7**, 205–224.

Triantafyllou, M. S., Triantafyllou, G. S. and Gopalkrishnan, R. (1991). Wake mechanics for thrust generation in oscillating foils. *Phys. Fluids A* **3**, 2835–2837.

Triantafyllou, M. S., Triantafyllou, G. S. and Yue, D. K. P. (2000). Hydrodynamics of fishlike swimming. *Annu. Rev. Fluid Mech.* **32**, 33–53.

Videler, J. J., Muller, U. K. and Stamhuis, E. J. (1999). Aquatic vertebrate locomotion: wakes from body waves. *J. Exp. Biol.* **202**, 3423–3430.

von Kármán, T. and Burgers, J. M. (1935). General aerodynamic theory. Perfect fluids. In *Aerodynamic Theory*, vol. II (ed. W. F. Durand), p. 308. Berlin: Springer-Verlag.

Wardle, C. S. and He, P. (1988). Burst swimming speeds of mackerel, *Scomber scombrus* L. *J. Fish Biol.* **32**, 471–478.

Webb, P. W. (1975). Hydrodynamics and energetics of fish propulsion. *Bull. Fish. Res. Bd. Can.* **190**, 1–159.

Webster, D. R. and Longmire, E. K. (1997). Vortex dynamics in jets from inclined nozzles. *Phys. Fluids* **9**, 655–666.

Wilga, C. D. and Lauder, G. V. (1999). Locomotion in sturgeon: function of the pectoral fins. *J. Exp. Biol.* **202**, 2413–2432.

Wilga, C. D. and Lauder, G. V. (2000). Three-dimensional kinematics and wake structure of the pectoral fins during locomotion in leopard sharks *Triakis semifasciata*. *J. Exp. Biol.* **203**, 2261–2278.

Willert, C. E. and Gharib, M. (1991). Digital particle image velocimetry. *Exp. Fluids* **10**, 181–193.

Wolfgang, M. J., Anderson, J. M., Grosenbaugh, M. A., Yue, D. K. P. and Triantafyllou, M. S. (1999). Near-body flow dynamics in swimming fish. *J. Exp. Biol.* **202**, 2303–2327.

Yuen, H. S. H. (1970). Behavior of a skipjack tuna, *Katsuwanus pelamis*, as determined by tracking with ultrasonic devices. *J. Fish. Res. Bd. Can.* **27**, 2071–2079.

Zar, J. H. (1984). *Biostatistical Analysis*. Englewood Cliffs, NJ: Prentice Hall.